# Stream sediment analysis for Lithium (Li) exploration in the Douro region (Portugal): A comparative study of the spatial interpolation and catchment basin approaches

Joana Cardoso-Fernandes [a,b,*], Jessica Lima [a,b], Alexandre Lima [a,b], Encarnación Roda-Robles [c], Martin Köhler [d], Stefan Schaefer [d], Andreas Barth [d], Andreas Knobloch [d], Mário A. Gonçalves [e], Filipe Gonçalves [a], Ana Cláudia Teodoro [a,b]

[a] Department of Geosciences, Environment and Spatial Planning, Faculty of Sciences, University of Porto, Rua Campo Alegre, 4169-007 Porto, Portugal
[b] ICT (Institute of Earth Sciences) – Porto Pole (Portugal), Rua Campo Alegre, 4169-007 Porto, Portugal
[c] Departamento de Geología, Universidad del País Vasco (UPV/EHU), Barrio Sarriena s/n, 48940 Leioa, Bilbao, Spain
[d] Beak Consultants GmbH, Am St. Niclas Schacht 13, 09599 Freiberg, Germany
[e] Departamento de Geologia and IDL, Faculdade de Ciências da Universidade de Lisboa, Edifício C6, Piso 4, Campo Grande, 1749-016 Lisboa, Portugal

## ARTICLE INFO

## ABSTRACT

Lithium (Li) was recently added to the list of critical raw materials by the European Union due to its significance for the green energy transition. Thus, the development of new toolchains to make Li exploration more economic and more effective is needed. Stream sediment analysis can play an important part in these new tool chains. In this work, two historical stream sediment datasets covering parts of the Fregeneda-Almendra pegmatite field in the Douro region (Portugal) were reprocessed considering two distinct approaches: spatial interpolation through inverse distance weighting (IDW) and the catchment basin approach using the concentration area (C-A) fractal analysis. The following objectives were delineated: (i) determine pathfinder elements for Li, considering relevant associations in the mineralization sources; (ii) compare the performance of both approaches; (iii) identify new target areas for Li. In the case of spatial interpolation, the highest Li values were associated to granites although the use of key elements allowed lithological discrimination and the delineation of target areas. In the catchment basin approach, fractal analysis proved to be effective in decreasing the number of areas of interest with high accuracy (>75%) when considering the previously mapped Li-pegmatites. One of the limitations identified was the number of anomalous basins related to the granites, despite the use of pathfinder elements allowing discriminating granite- from pegmatite-related Li anomalies. Comparing the two approaches, the spatial inter-polation method is more adequate for the early stages of exploration (reconnaissance), while the catchment basin approach is more suited for prospect-scale exploration. Field validation of the results identified one pegmatite containing Li mineralization and three others with favorable signs for Li mineralization in the Douro region.

## 1. Introduction

Stream sediment analysis and separation of anomalous samples from the background are a common and well-accepted tool employed in mineral exploration, especially to target metallic mineral occurrences, namely gold (Au) and copper (Cu), where the pathfinder elements and their mobility are well-known (Carranza and Hale, 1997; Cheng et al., 1994; Ghezelbash and Maghsoudi, 2018; Hawkes, 1976; Mokhtari and Garousi Nezhad, 2015; Shahrestani and Mokhtari, 2017; Zuo, 2011). Stream sediment sampling is mainly employed in the reconnaissance stage of an exploration campaign allowing to delineate target areas and to reduce the number of favorable regions to conduct more detailed studies in the subsequent exploration stages (Carranza and Hale, 1997; Mokhtari and Garousi Nezhad, 2015). The analysis of this source of data can either rely on spatial interpolation techniques that include moving averages or kriging techniques, for example (Ghezelbash et al., 2019;

---

Zuo, 2011), or on the sample catchment basin approach (Bonham-Carter et al., 1987; Mokhtari and Garousi Nezhad, 2015).

In the past decade, there has been an increasing demand for other raw materials that became essential for the green energy transition. This is the case of lithium (Li), which was recently considered critical by the European Union based on its economic importance and supply risk (European Commission: DG Internal Market Industry Entrepreneurship and SMEs, 2020). According to Kesler et al. (2012), the major hard-rock Li-deposits in Europe are hosted in pegmatites. Currently, there is only a few number of studies concerning the use of stream sediments to target pegmatite deposits, most of them related to lithium-cesium-tantalum (LCT) pegmatites (Dill et al., 2014; Frick and Strauss, 1987; Steiner, 2018). Kaeter et al. (2019) investigated tin (Sn), cesium (Cs), tantalum (Ta), and tungsten (W) stream sediment anomalies in Leinster (southeast Ireland), being Ta and Sn anomalies associated with LCT pegmatites. Similar studies showed the potential of combined geochemical and mineral approaches to stream sediment samples in the identification of anomalous Sn-W-Li-Cs-Ta geochemical associations related to granites in the Vosges Mountains, in northeast of France (Steiner, 2019; Steiner et al., 2019). Fyzollahhi et al. (2018) and Saadati et al. (2020) have successfully used stream sediment data for Li exploration in Iran to identify prospects related to both granitic rocks and pegmatites and sedimentary hectorite deposits. However, Li is a mobile cation, in contrast with Sn, Nb, and Ta which are immobile ions in stream sediments which might pose a constraint for the use of this kind of geochemical exploration technique (Rose et al., 1979). Despite this, other geochemical approaches, using agricultural soil samples, show that it is possible to identify areas of interest for high-tech elements such as Li at a continental scale, being most anomalous areas related to granites or LCT pegmatites (Négrel et al., 2019).

In the framework of the "Lightweight Integrated Ground and Airborne Hyperspectral Topological Solution" (LIGHTS; http://lights.univ-lorraine.fr/) project, one of the main aims is to create a toolchain to make Li exploration more economically sustainable and effective (Cardoso-Fernandes et al., 2020b; Köhler et al., 2021). To achieve this, historical stream sediment datasets covering the Douro region and the Portuguese portion of the Fregeneda-Almendra aplite-pegmatite field were reprocessed. Distinct methodological approaches employed by the project partners were confronted in this study. Additionally, to better understand the mobility of Li and related elements, this study compares for the first time the elemental associations observed in stream sediment samples with the ones observed at the mineralization source, i.e. pegmatite dykes and leucogranitic cupolas from the Iberian Peninsula. Taking this into account, the following objectives were defined for this study: (i) determine relevant pathfinder elements for Li in stream sediment samples; (ii) compare the results obtained with both spatial interpolation and catchment basin approaches and establish their utility in relation to traditional exploration stages; and (iii) delineate new Li prospects in the Douro region. Therefore, the findings presented in this work are a valuable contribution to the state of the art, since they can help in future and similar geochemical exploration campaigns for Li in other locations.

## 2. Study area and geological setting

The Li-mineralization in the Iberian Peninsula occurs along a belt with around 500 km in length and 150 km in width, mainly in aplite-pegmatite dykes but also in leucogranitic cupolas (Roda-Robles et al., 2016, 2018). This belt is located within the Central Iberian Zone (CIZ), which occupies a central portion of the Iberian Massif, one of the biggest and most complete fragments of the European Variscan Belt (Pérez-Estaún et al., 2004). The CIZ is mainly composed of a Neoproterozoic to Paleozoic metasedimentary succession, intruded by several Variscan granitoids (Martínez Catalán et al., 2004; Roda-Robles et al., 2018). Other important Li-occurrences are located in the Galicia-Trás-os-Montes Zone (GTMZ), a terrane accreted over the CIZ, that have similar

ages and features to those in the CIZ (GTMZ: 310 ± 5 Ma; CIZ: 301 ± 3 Ma by U—Pb dating of columbite-group minerals) (Melleton et al., 2011; Roda-Robles et al., 2016, 2018).

The Fregeneda-Almendra aplite-pegmatite field corresponds to one of the Li-occurrences within the CIZ (Fig. 1). The field is divided into two sectors: an eastern side in the Salamanca province (Spain) and a western sector in Vila Nova de Foz Côa (Portugal). This study focuses on the Portuguese side of the field, where historical stream sediment geochemical data is available covering not only the Portuguese sector of the pegmatite field, but also a larger extent of the Douro region. The Li-pegmatites are emplaced in the Douro Group (Sousa, 1982, 1983, 1984) of the Dúrico-Beirão Super Group (Silva et al., 1989), previously known as "Complexo Xisto-Grauváquico" (CXG) (Costa, 1950; Teixeira, 1955). The CXG corresponds to a monotonous pre-Ordovician pelitic-sandy flysch series of Upper Proterozoic to the Lower Cambrian age (Díez Balda et al., 1990; Rodríguez Alonso et al., 2004; Sousa, 1984). The series resulted from the accumulation of a thick sediment column (8000 m to 11,000 m), under a regime of tectonic instability, in a foreland type basin created by the CIZ's compartmentation in fault-delimited blocks, during the Cadomian orogeny (Rodríguez Alonso et al., 2004; San José et al., 1990). In its turn, the Douro Group corresponds to a stratigraphic succession, characterized by interlayered phyllites and metagreywackes with turbiditic features, divided into six different formations that are, from the base to the top: Bateiras, Ervedosa, Rio Pinhão, Pinhão, Desejosa, and S. Domingos (Sousa, 1982, 1983). Based on facies analysis, the basal formations present a distal turbiditic character, while the top formations present a proximal turbiditic character (Sousa, 1982, 1983). In the northeastern part of the study area, the Desejosa formation is overlayed by the Lower Ordovician quartzites from the Poiares' syncline and contacts with the alternating Ordovician quartzites and phyllites from the Castelo Melhor's syncline (Fig. 1) (Silva et al., 1990a,b; Silva and Ribeiro, 1991, 1994). To the south of the study area, a more local CXG formation was also identified – the Excomungada formation (Ribeiro, 2001; Ribeiro and Silva, 2000). This formation belongs to the Arda-Marofa group proposed by Silva et al. (1995) and represents the culmination of the sedimentation in the basin and is characterized by the presence of modified-wave turbidites sedimented in a siliciclastic platform with strong subsidence (Silva, 2005). The Excomungada formation is mainly composed of chloritic phyllites and quartzphyllites overlaying, by sedimentary progradation, upon the Rio Pinhão formation (Ribeiro and Silva, 2000; Silva, 2005). North of the Lower Ordovician quartzites from Poiares-Figueira de Castelo Rodrigo formation and the Middle to Upper Ordovician grey to black phyllites of the Santo Antão formation, the Excomungada formation suffered intense metamorphism (ultrametamorphism) leading to the formation of migmatites (Carvalhosa, 1960; Ribeiro, 2001; Ribeiro and Silva, 2000).

The metasedimentary sequences of the CXG were intruded by several granitoid rocks (Fig. 1), mainly in the south of the area, in the Figueira de Castelo Rodrigo–Lumbrales Anatectic Complex (FCR–LAC; Pereira et al. (2017)). These correspond essentially to *syn*-Variscan (concomitant with the third deformation phase – D3), S-type, two-mica granites ranging from fine- to coarse-grained, depending on the distinct facies (Ferreira et al., 2019; Pereira et al., 2017; Silva and Ribeiro, 1991, 1994). Fine-to-medium-grained, essentially biotitic, granodiorite is also present in the FCR–LAC (Ferreira et al., 2019; Ribeiro, 2001; Silva and Ribeiro, 1991, 1994), as well as some late-D3 two-mica granites with smaller cartographic expression (Silva and Ribeiro, 1991, 1994). Recent U—Pb zircon data show that the granitoids of the FCR-LAC yield ages between 300 and 317 Ma (Ferreira et al., 2019). The FCR-LAC exhumation was assisted by first-order shear zones (Ferreira et al., 2019; Pereira et al., 2017). In the northeast and northwest of the study area, the late- to post-D3 Saucelle and Freixo de Numão two-mica granites crop out (Silva and Ribeiro, 1991, 1994). Finally, a non-outcropping, leucocratic, fine-to-medium-grained with muscovite ≫ biotite granite was detected by drilling surveys between the Riba D'Alva mine and Feli mine (305.0 ± 3.3 Ma) (Vieira, 2010). Locally, there are several
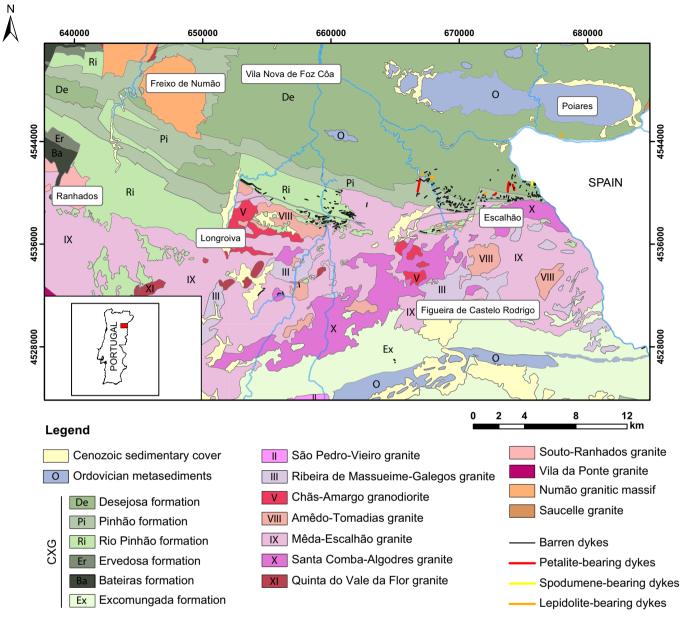
**Fig. 1.** Location of the study area and geological setting of the Portuguese side of the Fregeneda-Almendra aplite-pegmatite field, adapted from Carvalhosa (1960), Ribeiro and Silva (2000), Silva et al. (1990a,b) and unpublished geological data at the scale of 1:25,000. Roman numerals are from Ribeiro and Silva (2000). Location and classification of the Portuguese aplite-pegmatite dykes from Vieira (2010). Map projection: Universal Transverse Mercator zone 29N from the WGS84 datum.

Cenozoic sedimentary deposits including fluvial and slope deposits, alluvions, and fault-related arkoses covering both granitoids and metasediments (Silva and Ribeiro, 1991, 1994).

Regarding the Li-mineralization, there are four evolved dyke-types containing Li-minerals: (i) petalite-bearing aplite-pegmatites, (ii) spodumene-bearing aplite-pegmatites; (iii) lepidolite and spodumene-bearing aplite-pegmatites; and (iv) lepidolite-bearing aplite-pegmatites (Roda-Robles et al., 1999; Vieira, 2010). These are Li, F, Sn, Rb, Nb > Ta, B, and P enriched bodies (Roda-Robles et al., 1999; Roda, 1993; Vieira, 2010) that are emplaced in the CXG metasediments (Fig. 1). The mineral association includes quartz, feldspar, Li-muscovite, spodumene, petalite, cassiterite, montebrasite, and accessory apatite, Nb—Ta oxides, Fe—Mn phosphates, and eucryptite (Roda-Robles et al., 2018; Vieira, 2010; Vieira et al., 2011). Moreover, there are also several types of barren dykes, most emplaced within or near the granites of the FCR-LAC (Fig. 1). Therefore, there is an increasing fractionation degree to northwards as the distance to the granites increases (Vieira, 2010; Vieira

et al., 2011). Similarly, since the metamorphic isogrades are parallel to the granites' contact, barren dykes occur in the higher-grade metamorphic zones; petalite-bearing aplite-pegmatites only occur in the andalusite-sillimanite; and spodumene-bearing dykes are emplaced in the biotite and/or chlorite zones (Vieira, 2010; Vieira et al., 2011).

## 3. Data and methods

### 3.1. The stream sediment geochemical dataset

In this work, a previous geochemical stream sediment campaign covering the study area (>1250 km²) was reprocessed. The historical dataset was acquired in the early 1980s by the Douro consortium composed by the French Bureau de Recherches Géologiques et Minières (BRGM) and the Portuguese institution, Serviço de Fomento Mineiro (SFM). The dataset is composed of a regional campaign containing 3417 stream sediment samples, covering the 15-A, 15-B, and part of the 15-C

and 15-D sheets of the Portuguese Geological Maps at the scale of 1:50000 representing a density of four samples/km² (Viallefond, 1981; Viallefond and Angel, 1981). Moreover, there is a detailed, prospect-scale campaign in the Almendra region that was conducted for tin (Sn) and tungsten (W) exploration, where 298 samples were collected in a 43 km² area, representing an average density of about seven samples/km² (Angel and Viallefond, 1981). This smaller, prospect scale campaign covers various lepidolite- and petalite-bearing dykes including the Bajoca pegmatite (currently exploited as an open-pit mine), which corresponds to a petalite-bearing dyke that reaches 30 m in thickness and over 700 m in length (Almeida, 2003; Roda-Robles et al., 2010; Vieira, 2010). The regional campaign also covers known Li-mineralized dykes.

Similar sample collection and analytical procedures were employed in both regional and prospect scale campaigns. For the regional campaign, in each location, a sample of around 800 g. of fine sediments was collected off-stream. If the fine fraction was unavailable, gravel was sieved in situ to 1 mm particle size (Marroncle, 1980b). Each sample was divided into two equal parts, one for keeping and another to be dried at 30 °C in a muffle furnace. The dried part was then milled using a porcelain mortar and sieved to 100 mesh particle size (0.125 mm) in the laboratory (Marroncle, 1980b). From the sieved fraction, 20 g. were set aside as duplicate while around 40 g. of the sample were destined for geochemical analysis. Regarding the prospect scale campaign, the samples were previously collected off-stream, dried, and sieved to a particle size less than 80 mesh (0.177 mm) (Marroncle, 1980a; Viegas et al., 1983–85). All samples from the SFM and BRGM datasets were analyzed at the BRGM facilities using optical emission spectrometry or quantometer (Angel and Viallefond, 1981; Viallefond, 1981; Viallefond and Angel, 1981). This multi-element technique provided the simultaneous quantification of 34 elements and compounds, namely $SiO_2$, $Al_2O_3$, $Fe_2O_3$, MgO, CaO, $Na_2O$, $K_2O$, $TiO_2$, MnO, $P_2O_5$, Ag, As, B, Ba, Be, Bi, Cd, Co, Cr, Cu, La, Li, Mo, Nb, Ni, Pb, Sb, Sn, Sr, V, W, Y, Zn and Zr. However, the reports do not specify details on the digestion methods and analytical precision of the analyses.

### 3.1.1. Pre-analysis of the dataset

Before basin delimitation and anomaly definition, exploratory data analysis (EDA) was conducted. First, descriptive statistics of measured and log-transformed data were computed to understand the element distribution of both campaigns separately and as a whole (Table 1).

Additionally, graphic tools such as histograms, boxplots, and normal Q-Q plots were used. The analysis of the results shows that despite having similar trends for most elements, their distributions can differ between the two campaigns. Most of the elements/oxides have negatively skewed distributions (except Ba, $SiO_2$, $Al_2O_3$, $Fe_2O_3$, MgO, $Na_2O$, $K_2O$). However, BRGM shows element distributions more asymmetric than SFM except for $Fe_2O_3$, $Na_2O$, $TiO_2$, MnO, $P_2O_5$, Li, Be, and Nb. In both datasets, As, Sn, W, and Pb show a standard deviation higher than the mean. This is also the case of B, Cu, and Nb in the BRGM campaign. The SFM dataset shows: (i) a higher mean for Be, B, Cu, As, Sr, Sn, Ba, and W; (ii) higher standard deviation for $SiO_2$, $Al_2O_3$, $Fe_2O_3$, $TiO_2$, MnO, B, Cu, As, Sn, and W; (iii) a higher maximum content for $Fe_2O_3$, MgO, $TiO_2$, and MnO; and (iv) a higher minimum content for $Al_2O_3$, $Fe_2O_3$, MgO, CaO, $Na_2O$, $K_2O$, MnO, Be, B, Cu, Zn, Sr, and Ba. Moreover, the analysis of the results obtained with the graphical tools allowed to observe two populations in the distributions of: (i) As, Ba, Cu, Li, Sn, Sr, and W for both datasets, (ii) Pb and Zn for the SMF campaign, and (iii) Nb for the BRGM campaign. In the case of As, Li, Pb, Nb, Sn, and W, the first population is associated with values near the detection limit. For Sn and W, this population near the detection limit corresponds to the largest one. Also, for CaO, MgO, and Be, their respective distributions are almost exclusively related to values around the detection limit. Compared with the raw data, most element distributions approached a normal-like shape distribution after the logarithmic transformation. However, Be, $K_2O$, Nb, Sn, and W distributions did not change significantly after the transformation, Li distribution changed to positively skewed, and $Na_2O$ and $SiO_2$ distributions became more asymmetric. Overall, when analyzing Table 1, it is possible to recognize that the differences between the SFM and BRGM campaigns are usually residual, within ten potencies, and mainly corresponding to the differences in the geology of the area sampled.

In a second stage, the same EDA tools were used to understand how the elementary distributions changed according to the lithology. Overall, granites have higher values of $Na_2O$, $K_2O$, Li, Nb, and Sn when compared to metasedimentary rocks. Oppositely, the metasediments show higher contents of $Fe_2O_3$, B, Cu, Sr, Ba, and W when compared with granitoid rocks. The difference among samples located on granites and metasedimentary rocks is more prominent on the BRGM campaign, which has a higher number of samples. These differences in average concentrations are critical for the correct anomaly definition as demonstrated in the following chapters.

**Table 1**
Descriptive statistics for all the stream sediment samples and separate datasets. Min – minimum; Max – maximum; St. Dev. – standard deviation; Skew. – skewness.

| Element | All data (n = 3445) | | | | | Local campaign (SFM; n = 298) | | | | | Regional campaign (BRGM; n = 3417) | | | | |
|---|---|---|---|---|---|---|---|---|---|---|---|---|---|---|---|
| | Min | Max | Mean | St. Dev. | Skew. | Min | Max | Mean | St. Dev. | Skew. | Min | Max | Mean | St. Dev. | Skew. |
| $SiO_2$ (%) | 59 | 91 | 76.26 | 4.90 | −0.32 | 59 | 84 | 72.62 | 5.56 | −0.34 | 59 | 91 | 76.60 | 4.65 | −0.23 |
| $Al_2O_3$ (%) | 4 | 24 | 12.20 | 3.12 | 0.49 | 6 | 23 | 13.66 | 3.53 | 0.34 | 4 | 24 | 12.03 | 3.03 | 0.49 |
| $Fe_2O_3$ (%) | 1 | 11 | 3.95 | 1.63 | 0.19 | 3 | 11 | 5.68 | 1.57 | 0.53 | 1 | 8 | 3.82 | 1.53 | 0.03 |
| MgO (%) | 0.5 | 4 | 1.60 | 0.64 | 0.49 | 1 | 4 | 2.30 | 0.59 | 0.30 | 0.5 | 3 | 1.55 | 0.60 | 0.43 |
| CaO (%) | 0.5 | 8 | 0.55 | 0.24 | 12.51 | 0.5 | 1. | 0.53 | 0.13 | 3.48 | 0.5 | 8 | 0.55 | 0.24 | 12.54 |
| $Na_2O$ (%) | 0.1 | 3.6 | 1.88 | 0.62 | −0.10 | 0.5 | 2.6 | 1.56 | 0.29 | −0.20 | 0.1 | 3.6 | 1.89 | 0.63 | −0.16 |
| $K_2O$ (%) | 0.9 | 5.1 | 2.83 | 0.58 | 0.06 | 1.3 | 3.7 | 2.69 | 0.39 | −0.81 | 0.9 | 5.1 | 2.84 | 0.58 | 0.07 |
| $TiO_2$ (%) | 0.12 | 3.92 | 0.74 | 0.32 | 1.76 | 0.43 | 3.92 | 0.98 | 0.45 | 2.89 | 0.12 | 3.24 | 0.72 | 0.29 | 1.17 |
| MnO (%) | 0.01 | 0.31 | 0.05 | 0.03 | 2.20 | 0.02 | 0.40 | 0.08 | 0.05 | 3.40 | 0.01 | 0.27 | 0.05 | 0.02 | 1.70 |
| $P_2O_5$ (%) | 0.01 | 1.20 | 0.18 | 0.11 | 1.22 | 0.01 | 0.73 | 0.10 | 0.07 | 3.92 | 0.02 | 1.20 | 0.18 | 0.11 | 1.17 |
| Li (ppm) | 1 | 619 | 72.40 | 68.11 | 1.36 | 1 | 353 | 63.85 | 52.64 | 1.46 | 1 | 619 | 72.55 | 68.75 | 1.35 |
| Be (ppm) | 0.5 | 12 | 0.93 | 0.62 | 5.33 | 1 | 7 | 1.12 | 0.53 | 6.67 | 0.5 | 12 | 0.92 | 0.63 | 5.44 |
| B (ppm) | 7 | 1316 | 77.70 | 80.88 | 6.29 | 25 | 920 | 137.56 | 119.35 | 2.52 | 7 | 1316 | 74.41 | 76.61 | 6.94 |
| Cu (ppm) | 1 | 608 | 21.97 | 24.73 | 7.58 | 8 | 209 | 52.41 | 36.95 | 1.16 | 1 | 608 | 20.97 | 23.81 | 8.47 |
| Zn (ppm) | 32 | 2804 | 158.03 | 78.26 | 14.11 | 65 | 793 | 146.81 | 65.48 | 5.38 | 32 | 2804 | 158.01 | 78.25 | 14.62 |
| As (ppm) | 1 | 1589 | 43.42 | 97.64 | 6.73 | 1 | 1379 | 150.45 | 238.31 | 2.33 | 1 | 1589 | 35.34 | 71.65 | 8.16 |
| Sr (ppm) | 14 | 458 | 64.72 | 45.85 | 2.72 | 37 | 293 | 107.16 | 40.83 | 1.34 | 14 | 458 | 61.89 | 44.43 | 3.06 |
| Nb (ppm) | 1 | 137 | 2.31 | 4.69 | 9.17 | 1 | 16 | 1.05 | 0.87 | 17.26 | 1 | 137 | 2.37 | 4.79 | 8.98 |
| Sn (ppm) | 1 | 139 | 3.27 | 5.62 | 9.42 | 1 | 101 | 4.18 | 8.57 | 6.29 | 1 | 139 | 3.18 | 5.23 | 9.88 |
| Ba (ppm) | 21 | 2017 | 285.79 | 148.65 | 0.86 | 141 | 667 | 396.83 | 101.20 | 0.47 | 21 | 2017 | 277.20 | 146.13 | 0.99 |
| W (ppm) | 1 | 1034 | 4.17 | 32.60 | 19.46 | 1 | 786 | 20.58 | 67.99 | 6.71 | 1 | 1034 | 2.86 | 26.80 | 26.75 |
| Pb (ppm) | 1 | 3000 | 19.14 | 77.08 | 33.00 | 1 | 724 | 24.80 | 51.76 | 9.18 | 1 | 3000 | 18.45 | 77.68 | 33.75 |

Finally, association measures such as Pearson's and Spearman's correlation coefficients and multivariate analysis techniques such as Cluster analysis and Principal Component Analysis (PCA) were also employed to determine relevant element associations with Li. Both the Pearson's and Spearman's correlation coefficients were employed to analyze different element associations within the geochemical datasets: (i) the Pearson's coefficient allows evaluating linear correlations while (ii) the Spearman's coefficient measures monotonous associations between variables. Moreover, the Spearman coefficient is a non-parametric measure and therefore is not affected by the presence of outliers in the populations (unlike the Pearson's coefficient). Therefore, the two measures were employed as an exploratory tool to evaluate any kind of relevant element association to be further employed in the multivariate statistical analysis. When considering the raw data from both datasets, for most elements the correlation with Li is negligible (Pearson $r < 0.3$), but $P_2O_5$ showed a moderate correlation with Li ($0.5 \leq$ Pearson $r < 0.7$), while $K_2O$, $Na_2O$, $Al_2O_3$, Sn, Be, and As show weak correlations ($0.3 \leq$ Pearson $r < 0.5$; thresholds from Mukaka (2012)). Nevertheless, the element associations are distinct for each campaign. In the SFM campaign, a weak correlation (based on Pearson's coefficient) was found between Li and Sn, As, Be, $K_2O$, B, and Pb. Considering Spearman's coefficient, the correlation with Sn, Pb, and As is moderate and there is an additional weak correlation between $P_2O_5$, W, and Li. For the BRGM campaign, there was only a moderate correlation between Li and $P_2O_5$, and weak correlations with $K_2O$, $Na_2O$, $Al_2O_3$, Sn, As, Be, when using the Pearson association measure. With Spearman's coefficient, there is also a weak correlation between Li and Zn, and the correlation with Sn, $K_2O$, and

$Na_2O$ increases to moderate. This shows that the Spearman's coefficient allowed to identify associations not highlighted by the Pearson's coefficient and, for several elements, there are changes in the strength of the associations.

The multivariate analysis was only employed for the Li-correlated elements, after standardization using the interquartile range (IQR), following Eq. (1):

$$Z_{ij} = \left( X_{ij} - median_j \right) / IQR_j \tag{1}$$

where $Z_{ij}$ corresponds to the standardized value for population j, and $X_{ij}$ is the original value i in population j. Fig. 2 shows the effect of the standardization on oxide/element distribution.

### 3.2. Geochemical pathfinder analysis

The same multivariate statistical analysis (described in Section 3.1) was employed to determine relevant element associations in the Li-mineralization sources in the Iberian Peninsula. For this particular purpose, an external geochemical dataset was used, containing a total of 168 whole-rock analyses from lepidolite-rich ($n = 41$), spodumene/petalite-rich ($n = 25$), and simple aplite-pegmatite dykes and leucogranitic cupolas ($n = 102$). The available geochemical dataset consists of 37 analyses performed by Roda-Robles et al. (2018), while the remaining analyses were compiled by the same authors based on existent research about the Argemela, Castillejo de Dos Casas, and Pinilla de Fermoselle lecogranitic cupolas, and about the Barroso-Alvão,
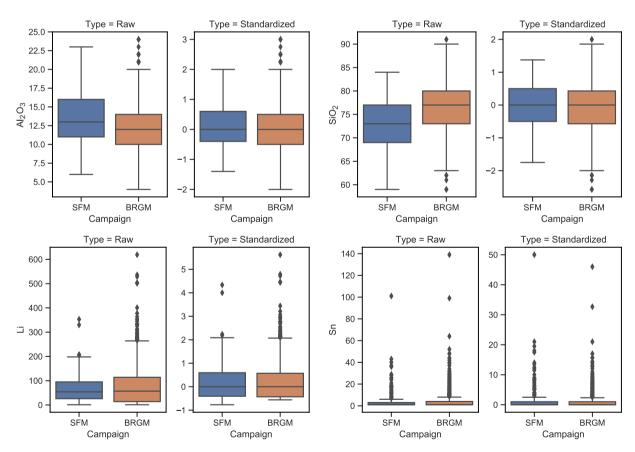


**Fig. 2.** Boxplot comparing selected oxide/element distributions before and after standardization using the IQR method (Eq. (1)), for both SFM and BRGM campaigns. For the raw data, oxides are in weight % and elements are in ppm. In the case of cluster analysis, the distance metric employed was always the Euclidian distance, but different linkage methods were tested (Ward's, single, complete, average, centroid, and median). The cophenetic correlation coefficient was computed to evaluate the hierarchical clustering. The dendrograms' cutoff value was set to the median of the third-from-last and second-from-last linkages. Moreover, PCA was employed on both Pearson's and Spearman's correlation matrices for Li-correlated elements. The dendrograms evidenced a Li-$K_2O$-B-As-$P_2O_5$ cluster for the SFM campaign and a Be-$Al_2O_3$-$K_2O$-$Na_2O$-Li-$P_2O_5$ for the BRGM dataset. PCA revealed more complex associations, but overall there are associations between Li and Pb, As, Sn, $K_2O$, and $P_2O_5$ in the SFM campaign, and associations between Li and $P_2O_5$, $Na_2O$, $K_2O$, Sn, Be, and As in the BRGM dataset.

Fregeneda-Almendra, Gonçalo, Lalín-Forcarei, Las Navas, Segura, Seixoso-Vieiros, Serra de Arga, Jalama, and Tres Arroyos pegmatite-fields (Almeida, 2003; Antunes et al., 2013; Charoy and Noronha, 1996; Fuertes Fuente and Martin Izard, 1998; Gallego Garrido, 1992; Helal, 1992; Leal Gomes, 1994; Martín-Izard et al., 1992; Neiva and Ramos, 2010; Roda-Robles et al., 2012; Von Knorring and Vidal Romani, 1981). In this work, the whole-rock data were only employed for the determination of relevant pathfinders.

As a consequence of the very heterogeneous whole-rock geochemistry dataset (distinct analytical packages for each studied location), two subsets were considered in the multivariate analysis to create a balance between preserving the largest number of samples and elements possible: i) 100 analyses for 16 elements ($Al_2O_3$, CaO, $Fe_2O_3$, $K_2O$, MgO, $Na_2O$, $P_2O_5$, $SiO_2$, Ba, Cs, Li, Nb, Rb, Sn, Sr, Ta); ii) 51 analyses for 22 elements ($Al_2O_3$, CaO, $Fe_2O_3$, $K_2O$, MgO, MnO, $Na_2O$, $P_2O_5$, $SiO_2$, $TiO_2$, Ba, Cs, F, Ga, Nb, Rb, Sn, Sr, Ta, Zn, Zr). For additional information on the external whole rock dataset, please refer to Roda-Robles et al. (2018) and references therein. The correlation analysis was employed on the entire whole-rock geochemical dataset.

The multivariate approach allowed defining a general Li-Rb-F-Sn-Cs-$Al_2O_3$-$K_2O$-MnO association. The multielement associations can vary according to the chosen subset and technique. For the first subset, cluster analysis evidenced a $K_2O$-Rb-Sn-Li-$Al_2O_3$-$Na_2O$ association similar to the Rb-Cs-Li-Sn-($Al_2O_3$) association identified through PCA (-A). In the second subset, an $Al_2O_3$-$K_2O$-MnO-Zn-Sn-Li-Rb-F cluster was observed (-B) while PCA highlighted an F-Cs-Li-Rb-Sn-MnO-(Zn) association. In detail, for the first dataset, the first three principal components (PCs) explain almost 95% of the observed variance: (i) PC1 explains 61.8% of the total variance, representing a $Na_2O$-$SiO_2$-$Fe_2O_3$-Ba association antipathetic with a Li-Rb-Cs-Sn association; (ii) PC2 explains 27.5% of the total variance and is dominated by $Al_2O_3$-$Na_2O$ association antipathetic with $K_2O$-$SiO_2$; and (iii) PC3 explains a smaller portion of the total variance (5.6%), representing a weak association between $SiO_2$-$Na_2O$ antipathetic with $Fe_2O_3$ and Ba. By plotting the loads of each PC into distribution diagrams (Fig. 3-A), it is easier to observe element associations. For example, although there is a clear Li-Cs-Rb-Sn association, it is visible that the association between Li and Sn has less strength than with Cs or Rb (Fig. 3-A). This and the remaining associations observed in the distribution diagram of Fig. 3-A are interpreted as reflecting the control of distinct mineral assemblages within the analyzed pegmatites and leucogranitic cupolas of Iberia. Similarly, for the second dataset, the dendrogram of Fig. 3-B is the visual representation of the hierarchical clustering of the distinct geochemical variables. Therefore, related geochemical variables (with linkage distances below the defined threshold) are grouped together in the same clusters. In this case, Cs is no longer grouped with Li and forms a cluster separated from the remaining variables. On the other hand, there is an important association between Li and F in Cluster 3, although the relation with MnO or Zn is more difficult to explain and interpret. Finally, Spearman's correlation measure also identified a weak correlation between Li and B. In a preliminary study where only Li-rich pegmatites and leucogranitic cupolas were considered (Cardoso-Fernandes et al., 2020a), a strong correlation was found with B, but the correlation between Li and Sn was not as relevant as the one observed using the whole dataset.

Overall, B together with Rb, Sn, Cs, and F are common elements that define the geochemical signature of the Rare-Element pegmatite class, namely of Li-rich pegmatites worldwide (Černý and Ercit, 2005; Simmons and Webber, 2008). However, no association was found with other typical elements found in Li-rich bodies such as Ta and Nb (Černý and Ercit, 2005; Roda-Robles et al., 2018; Simmons and Webber, 2008). This could be explained by difficulties in acquiring representative samples for the accessory Ta—Nb phases or it could reflect the occurrence of a nugget effect (Cardoso-Fernandes et al., 2020a). Although Be could also be an important pathfinder element for Li-mineralizations, no association with Li was found through the multivariate approach which would be expected since beryl is less common in the Li-rich bodies of the Iberian Peninsula (Cardoso-Fernandes et al., 2020a; Roda-Robles et al., 2018). Finally, the association between Li and major oxides such as MnO, $K_2O$, and $Al_2O_3$ can be explained by the co-occurrence of Mn oxides in Li-rich bodies of the CIZ-GTMZ and due to the presence of K and Al in the structure of Li-minerals (Cardoso-Fernandes et al., 2020a; Roda-Robles et al., 2018).

Next, a correspondence between the Li-correlated elements in the Li-rich bodies of the CIZ-GTMZ and the elements available in the stream sediment datasets was made. Comparing these results with the ones obtained in Section 3.1, it is evident that the Li association with elements such as Pb or As in the stream sediment samples do not represent the typical associations found in Li-rich bodies. Despite elements/oxides such as Be and $P_2O_5$ (that show a positive correlation with Li in the stream sediment dataset) may be present in Li-pegmatites, there was no significant correlation with Li in the CIZ's Li-rich bodies. Important pathfinders for Li-pegmatite exploration, namely Rb, Cs, and F were not analyzed in the stream sediment campaigns. Nonetheless, other relevant pathfinders can be used to pin-point Li-pegmatites in the Douro region: Sn, B, $Al_2O_3$, MnO, and $K_2O$. All these pathfinder elements have shown correlations with Li in both CIZ's Li-rich bodies and the stream sediment samples.
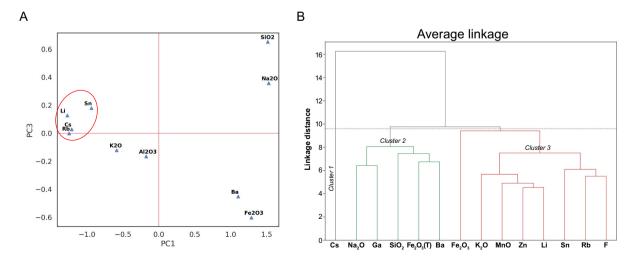


**Fig. 3.** Multivariate analysis for the identification of associations in Li-rich bodies from the CIZ-GTMZ: (A) Projection of the selected elements/oxides loadings on the plane PC3 vs PC1 for the first subset ($n = 100$); (B) Dendrogram showing the hierarchical clustering of selected elements/oxides for the second subset ($n = 51$).

### 3.3. Automatic extraction of drainage network and basin creation

The extraction of the drainage network was performed automatically using ArcGIS Spatial Analyst tools (Hydrology and Conditional menus) (Environmental Systems Research Institute, 2020). Different data sources covering the study area and methods were applied to determine which combination was more effective (Table 2).

For each pair of data source/extraction method, the number of streams, total length of streams, and drainage density were calculated. The drainage density was calculated by dividing the total stream length by the area in which the drainage network was extracted. For the drainage networks extracted with the stream order method, it was also computed for each order the number of streams, their length, and the drainage density. In this case, the drainage density was calculated by dividing the length of streams in each order by total area. The drainage network chosen was the one obtained using the DFM and the Stream Order method, since it presented the least number of artifacts.

Each sampling point was manually corrected to intersect the extracted drainage network, but always considering the original sampling maps from the 1980s. Basin creation was performed using the *Watershed* tool in the Hydrology menu (ArcGIS Spatial Analyst tools), which takes into account the flow direction as well as the stream sediment points. However, the automatically delineated catchment basins presented major topology problems (Fig. 4) such as: (i) polygons without true catchment area, (ii) existing polygons of major streams, and (iii) many polygon artifacts (irregular shapes or smaller catchment basins inside larger ones). Most of the identified problems are related to the resolution of the primary raster data set. The following correction of catchment data was done through: (i) improvement of the drainage network and contour line creation for data validation; (ii) position correction of the stream sediment samples; (iii) manually correction of irregular polygons; and (iv) catchment basins related to major streams ($>1.5$ km$^2$) were excluded from the dataset due to their low representativeness since these samples correspond to a mixed signal and it is not possible to assign a source (due to a large number of tributaries in the upper course).

### 3.4. The spatial interpolation method

Since the interpolation method is not dependent on the catchment area and the differences between the SFM and BRGM populations are mainly due to changes in lithology, it was possible to treat the two campaigns together. In preparation, the SFM and BRGM datasets were merged (after comparison of values) and overlapping polygons were adjusted. The values/units for the elements of interest (Li, Sn, W, As, etc.) were harmonized (% into mg/kg) and logarithmized. In the next step, the center of each polygon was projected using the Feature to Point-tool in ArcGIS v10.6 software.

In this work, to analyze the stream sediment data and estimate elemental concentrations in unsampled areas the inverse distance weighting (IDW) was employed. IDW is one of the most used moving-average interpolation techniques, with the advantage of intuitive and straightforward implementation (Carranza, 2009a; Ghezelbash and Maghsoudi, 2018; Spadoni, 2006; Zuo, 2011). The interpolation method estimates unknown values between known values based on the assumption that closer values are more related than distant values (Shepard, 1968). Taking this into account, a weight (power coefficient) is assigned to each known point used in the prediction of unknown points that will decrease with the distance (Johnston et al., 2004).

In this work, the IDW interpolation was conducted with a cell size of $20 \times 20$ m, exponent of distance (power) of 2, and a search radius of 20 m. The catchment centers represented the reference points for the interpolation using IDW. To limit the interpolation area, the center points were buffered by 1000 m, a polygon was assembled from all the single buffer polygons, and the edge of the resulting polygon was used as a mask. The interpolation itself was done using ArcPy running on ArcGIS 10.6 and the results were saved as a raster file format. Besides Li, other elements were interpolated via the IDW method, namely As, Sn, and Cu. These elements were selected based on the interrelationship with Li in the stream sediment dataset and the potential for lithological discrimination previously evaluated in Section 3.2.

### 3.5. The catchment basin method

Unlike the spatial interpolation approach, for the catchment basin method, the two campaigns (BRGM and SFM) were treated separately due to different sampling densities and distinct element distributions observed in the two populations. Since this approach relies on several area-dependent calculations, it is crucial to treat the campaigns independently.

### 3.5.1. Determination of the lithological background and dilution correction

Because lithological variations can have a great influence on element content in each sample, it is necessary to estimate the background concentration of each lithologic unit. This is particularly important since, as stated in Section 3.1, the granites are more enriched in elements such as Li, Cs, Rb, Nb, and Sn when compared to the metasedimentary units (Ferreira et al., 2020; Roda-Robles et al., 2018). The lithological background was estimated through the weighted average method which considers the area of lithologic units in every sample catchment basin (Bonham-Carter et al., 1987; Carranza, 2009b; Carranza and Hale, 1997). The local background content due to lithology in every sample catchment basin was then estimated in two steps. First, a weighted average element concentration $M_j$ ($j = 1, 2... m$) for the jth ($j = 1, 2... n$) lithologic units was determined using Eq. (2) (Carranza, 2009b):

$$M_j = \sum_{i=1}^{n} C_i A_{ij} \bigg/ \sum_{i=1}^{n} A_{ij} \qquad (2)$$

where $A_{ij}$ is the area of the jth lithologic unit in the sample catchment basin i ($i = 1, 2... n$), $C_i$ represents the element concentration of the sample at the basin outlet, and the sum term in the denominator is the total area of lithology j. Then, the local background concentration of the element ($C'_i$) due to lithology was estimated through Eq. (3) (Carranza, 2009b):

$$C'_i = \sum_{j=1}^{m} M_j A_{ij} \bigg/ \sum_{j=1}^{m} A_{ij} \qquad (3)$$

where the sum term in the denominator is equal to the total area of the ith sample catchment. The estimated local background values for every lithological unit in the SFM and BRGM campaigns are presented in Appendix A, Tables A1 and A2, respectively.

Finally, another key aspect to consider when applying the catchment method is the dilution effect which results from the mixing of eroded
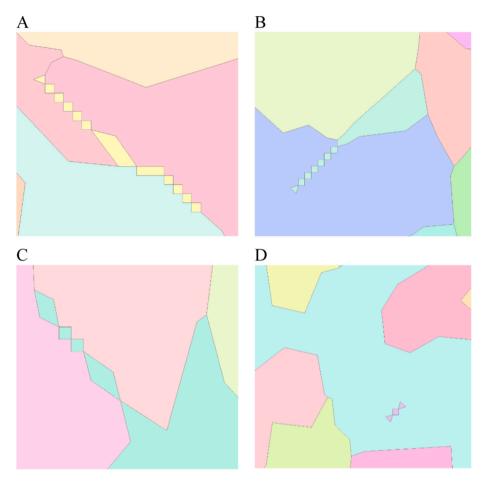
**Table 2**
Description of the distinct data sources and drainage extraction methods employed.

| Data source | Resolution | Extraction method | Description |
|---|---|---|---|
| Digital Elevation Model (DEM) | 20 m | Set Null | A threshold is applied to the flow accumulation model and only the cells with a flow accumulation higher than the stipulated threshold are classified as part of the drainage network. |
| Digital Flow Model (DFM) | 25 m | Stream Order | The stream segments are classified based on the number of upstream tributaries (Strahler, 1952). Stream order only increases when streams of the same order intersect. |

**Fig. 4.** Examples of basin artifacts that had to be manually corrected: (A–D) irregular polygon shapes; (D) smaller catchment basin inside a larger one.

sediments from non-anomalous locations with sediments from mineralized sources (Carranza and Hale, 1997; Hawkes, 1976; Mokhtari and Garousi Nezhad, 2015). Both the Hawkes' (Eq. (4), when n equals 0) and the Hawkes' modified methods (Eq. (4)) were evaluated for the dilution correction, considering that the dilution effect is a function of the catchment area and that the area of the mineralized source (pegmatite) is negligible (0.01 km$^2$):

$$C_a = (100A_i)^{1+n}(C_i - C_i')$$ (4)

where $C_a$ represents element concentration due to anomalous sources, $A_i$ is the area of the catchment basin, $C_i$ corresponds to the measured concentration of the element at the basin outlet, $C_i'$ represents the lithological background value of the element, and n corresponds to arbitrary equidistance values of 0, −0.25 and −0.5 (Carranza and Hale, 1997; Hawkes, 1976; Mokhtari and Garousi Nezhad, 2015). The final term of Eq. (4) represents the uni-element residuals. In this work, the residuals were standardized through the IQR method (Eq. (1)) before the dilution correction as suggested by Carranza (2009b). The best results were obtained with the original Hawke's equation (*n* = 0).

*3.5.2. Anomaly definition through fractal analysis*

Several statistical techniques are available to separate and classify geochemical anomalies from the background population, namely the percentile method (Carranza, 2004), the median absolute deviation (Shahrestani and Mokhtari, 2017), or fractal analysis (Fyzollahhi et al., 2018; Mokhtari and Garousi Nezhad, 2015). However, the concentration-area (C-A) fractal method proposed by Cheng et al. (1994) is one of the most popular methods for the definition of geochemical anomalies (Ghezelbash et al., 2019; Gonçalves et al., 2001). With the C-A method,

for each concentration threshold there is a corresponding occupied area with values greater than the threshold (Cheng et al., 1994). The fractal dimensions correspond to the slopes of the straight lines fitted by the least square method on the log-log plot of A(ρ) versus ρ (Carranza, 2009a). Breaks between straight-line segments on the log-log plot determine the thresholds between distinct geochemical populations (Carranza, 2009a; Cheng et al., 1994).

In this study, the C-A fractal method was employed to identify uni- and multi-elemental anomalies in each stream sediment dataset. For this, the diluted-corrected residuals of Li and the diluted-corrected residuals of the remaining pathfinder elements (list of elements available in Section 3.2) were used. The area was estimated through the box-counting method where a grid with distinct cells was superimposed on the areas covered by each campaign (Cheng et al., 1994). Different cell sizes were tested, ranging from the computed average nearest neighbor (avgnn) to a maximum of 2.5 times the avgnn, in equally spaced intervals.

In the case of uni-elemental anomaly determination, the chosen cell size for the box-counting method was 443.32 m and 140.54 m, and the number of concentration classes was 35 and 30 for the BRGM and SFM campaigns, respectively. Different populations and thresholds were recognized in the C-A log-log plots (representative graphs are presented in Appendix B, Fig. B1-A, B).

In what concerns the multi-element anomaly definition, only the stream sediment samples with positive diluted-corrected residuals at least for Li were selected, as suggested by Carranza (2009b), to ensure that the element associations related to the background population were not mapped. A rank-ordering approach was employed to the n positive diluted-corrected residuals, assigning descendent ranks from n to 1 (with averaged tied ranks) to after applying a Spearman rank correlation

matrix on the rank-transformed diluted-corrected residuals (Carranza, 2009b; Carranza and Hale, 1997; George and Bonham-Carter, 1989). Finally, the PCA was carried out on the resultant Spearman correlation matrix of the stream sediment samples with positive diluted-corrected residuals at least for Li. The existing multi-element associations on each PC were evaluated based on the resultant eigenvector loadings, allowing the selection of key PCs for Li-exploration (Appendix B, Tables B1 and B2). As observed, the selected PCs explained most of the total variance of the datasets (around 91% for the SFM campaign and around 97% for BRGM). Also, the values highlighted in bold in Tables B1 and B2 represent key positively or negatively correlated geochemical variables with each PC, with values close to one representing high correlations and values close to zero representing irrelevant or non-existing correlations. This means that, for SFM, Li is highly and positively correlated with PC2 while Sn is weakly and positively correlated (Table B1). In the case of PC1, B is highly positively correlated, and Sn is moderately and positively correlated. For the BRGM campaign, Li is correlated moderately and positively with PC4, while Sn is correlated moderately and negatively with PC2 (Table B2).

Afterward, the PC scores of the rank-transformed dilution-corrected stream sediment residuals were computed according to Eq. (5) (George and Bonham-Carter, 1989):

$$S_{ci} = \sum_{j=1}^{k} L_{cj} r_{ij} \qquad (5)$$

where $S_{ci}$ corresponds to the score for sample i (=1,2, …, n) on PC c, $L_{cj}$ is the loading of variable j (=1,2, …, k) on PC c, and $r_{ij}$ is the rank of sample i for variable j. The resultant scores were plotted along with the geochemical variables on the PCA biplots of Fig. B2 (Appendix B). The biplots allow to quickly understand the relation between the geochemical variables, stream sediment samples, and the selected PCs. For example, Li is most correlated with PC2 for SFM (Fig. B2-A) and with PC4 for BRGM (Fig. B2-B), due to the small angle between the Li vector and the respective PC axes, which is in accordance with Tables B1 and B2. Also, the length of the vectors (arrows) provides information on the proportion of variance explained by the two PCs for that variable. For SFM (Fig. B2-A), the length of the vectors is similar, meaning that PC1 and PC2 contain considerable information on all geochemical variables, while for BRGM (Fig. B2-B), the Li vector shows the greatest length, followed by MnO and Sn, which means that these variables are well represented by PC2 and PC4. Moreover, the angle between variable vectors provides insights on the correlation between variables: (i) for SFM (Fig. B2-A) Li is positively correlated with Sn, Sn is strongly and positively correlated with B, due to the small acute angle, and Li is weakly negatively correlated with B, due to the obtuse angle between the respective vectors; (ii) for BRGM (Fig. B2-B) it is visible that Li has a very low correlation with Sn because the respective vectors are almost orthogonal. Finally, biplots can also be useful to visualize clusters or groups of samples evidenced by the PCA transformation. In this case, it was not possible to distinguish separate, independent clusters, although stream sediment samples with high rank values are more frequently plotted in the positive quadrants of PC2 for SFM (Fig. B2-A) and PC4 for BRGM (Fig. B2-B).

Lastly, the individual PC scores were subjected to the C-A fractal analysis. Taking into account the PCA matrices and biplots (Tables B1, B2, and Fig. B2) and to better define multi-element anomalies, two PCs of interest were integrated (through multiplication), after normalization of the individual scores, and before fractal analysis. The process to decompose the multi-elemental stream sediment anomalies from the background was similar to the one employed for uni-element anomaly definition. The number of concentration classes was the same for each campaign, but due to a smaller number of samples, the cell size used in the box-counting method changed to 576.47 m and 192.56 m for the BRGM and SFM, respectively. The representative log-log plots are shown in Appendix B, Fig. B1-C, D.

### 3.6. Field validation

Two portable pieces of equipment were used to assess the dykes' potential to be mineralized in Li, namely the S1 Titan 600 portable X-Ray Fluorescence (XRF) from Bruker and Z300 Laser-Induced Breakdown Spectroscopy (LIBS) from SciAps© instruments. The former was employed to measure the content of Rb in potassium (K) feldspar crystals since the enrichment in this metal during crystallization reflects the fractionation degree of the pegmatites and consequently, their economic potential for Li (Cerny et al., 1985; Smeds, 1992). A threshold of 2000 ppm was set to discriminate the more evolved dykes with the potential to bear Li minerals (Ribeiro et al., 2018). The XRF equipment works with a rhodium anode and an excitation source of 4 W, with a voltage of 15 to 50 kV and a current of 5 to 100 µA. A factory calibration for $K_2O$ and Rb has a detection limit of 55 ppm and 1 ppm, respectively, when operating with the GeoExploration mode according to the manufacturer. The XRF performance has been tested against certified samples in previous work (Ribeiro et al., 2018). On the other hand, the portable LIBS was employed to assess the Li content on micas and to confirm the existence of Li aluminum silicates (petalite or spodumene), using two specific in-house calibrations for the GeoChem mode, or phosphates (montebrasite-amblygonite), through the equipment's Element-Pro elemental detection method. The SciAps Z-300 spectrometer range goes from 190 to 950 nm (Li peaks are located around 610 and 670 nm), with a laser excitation source of 5 to 6 mJ/pulse, 10 to 50 Hz repetition rate and uses argon at 13 psi as a purge gas. More information on the use of the LIBS equipment and its use to analyze Li-rich minerals can be found in Fabre et al. (2021).

## 4. Results and discussion

### 4.1. The spatial interpolation approach

The final interpolation maps created with IDW are presented in Fig. 5. As visible in Fig. 5-A, the highest Li values are mainly related to the granites from the Numão Massif (top left corner) and the FCR-LAC (E-W belt), thus outlining a major structural feature – the Vilariça Fault zone. Nonetheless, there is also a high Li-value area near the Riba D'Alva mine, where lepidolite dykes are known (top right corner, below the Poiares syncline). In the Almendra region, covered by the SFM campaign (highest density of sampling), where several Li-rich dykes are mapped, an enrichment in Li is noticeable. However, this enrichment is overshadowed by the Li content of the granites to the south. Pathfinder elements, such as Sn (Fig. 5-B), proved to be useful in the delineation of target areas. Despite some anomalies related to granites (especially to the East), it is possible to delineate three smaller areas of interest: (i) near the Riba D'Alva mine, (ii) near Almendra (coinciding with a known petalite-rich dyke exploited in the Bajoca mine), and (iii) near Castelo Melhor (south of the area not sampled) where there are no known pegmatites. Important As enrichments were observed (Fig. 5-C) in the Castelo Melhor and Riba D'Alva areas, as well as in the granites to the East. Intermediate As contents were observed in Almendra. Finally, the interpolation of elements such as Cu (Fig. 5-D), proved to be helpful for lithological discrimination. As seen in Section 3.1, the metasedimentary rocks present higher Cu contents compared to granitoid rocks, thus allowing to properly discriminate the granites from the FAR-LAC. Oppositely, the granites from the Numão Massif show a higher Cu content not allowing their discrimination.

Elemental interpolation using the IDW method turned out to be a simple and expeditious approach. Overall, the results show the influence that granitoids have on the Li content and proper definition of interest areas. This influence could be reduced through masking (using the existent geological maps) or the removal of lithological background (as performed in the catchment basin approach) prior to interpolation. Notwithstanding, the use of key pathfinder elements also allowed to decrease the granites' impact and was crucial to delineate target areas. In
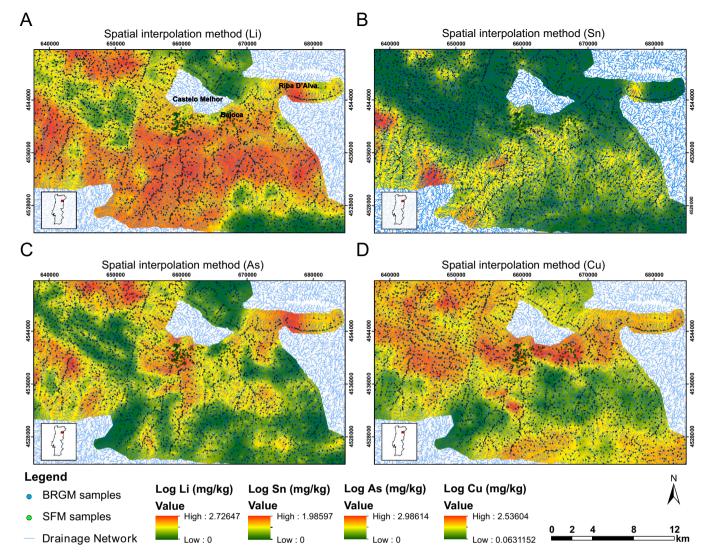
**Fig. 5.** Final interpolation maps obtained with the IDW: (A) Li; (B) Sn; (C) As; and (D) Cu. The location of the stream sediment samples is also shown.

previous studies focusing on Li exploration through stream sediment analysis, interpolation techniques were also used to estimate the distribution of relevant factor scores of geochemical samples (Fyzollahhi et al., 2018; Saadati et al., 2020). The authors have concluded that such an approach is effective for reconnaissance campaigns and regional exploration (Saadati et al., 2020). The results obtained in this work also indicate that the interpolation approach is more suitable for early stages of exploration that focus on a regional (or district) scale since the inherent smoothing of the anomalies results in a loss of detail that is crucial in the final stages of exploration.

### 4.2. The catchment basin approach

As mentioned before, the two campaigns were treated separately in this approach. In the first stage, only uni-elemental anomalies were determined. The anomalous catchment basins for Li are depicted in Fig. 6, where both campaigns are presented. In the case of BRGM, 68 out of 3362 basins were identified as anomalous, which corresponds to approximately 2% of all basins. This indicates that the C-A fractal method was effective in reducing possible interest areas to visit in the field, and thus the duration and costs of field campaigns, which is of particular interest for exploration companies. Some of the anomalies shown in Fig. 6 correspond to the Riba D'Alva area or are related to known pegmatite dykes North of Escalhão (near the border with Spain).

Table 3 summarizes the performance of the catchment basin approach, with the C-A fractal method achieving an overall accuracy (OA) of 93% considering the overlap of anomalous basins with known Li-pegmatites. Despite this, a large number of anomalous basins are still related to the outcropping granites, which is one of the main limitations found. After the removal of the lithological background, it was expected to eliminate the influence of granitoid rocks. Although it was not possible to eliminate their influence altogether, the impact of granites was reduced when compared with the spatial interpolation results (Fig. 5-A).

For the SFM campaign, 22 out of 289 basins were identified as anomalous (approximately 7.6%). The higher percentage of anomalous basins is a consequence of the lower threshold identified in the log-log plot (Fig. B1-A). It also might be related to the smaller size of the basins, meaning that one source can contribute to multiple basins as observed around the Bajoca pegmatite (red triangle on the bottom of Fig. 6). There is still some influence of granitoid rocks (resulting in anomalous basins) that is a result of the lower estimated lithological backgrounds for granites (Tables A1 and A2). This is linked with fewer availability of samples covering granites in the SFM campaign. Looking at Table 3, the OA of the fractal analysis drops to 75%. To improve these results, pathfinder elements were employed for multi-element definition.

The anomalous multi-element associations are represented in Fig. 7. For the BRGM campaign, the number of highly anomalous basins,
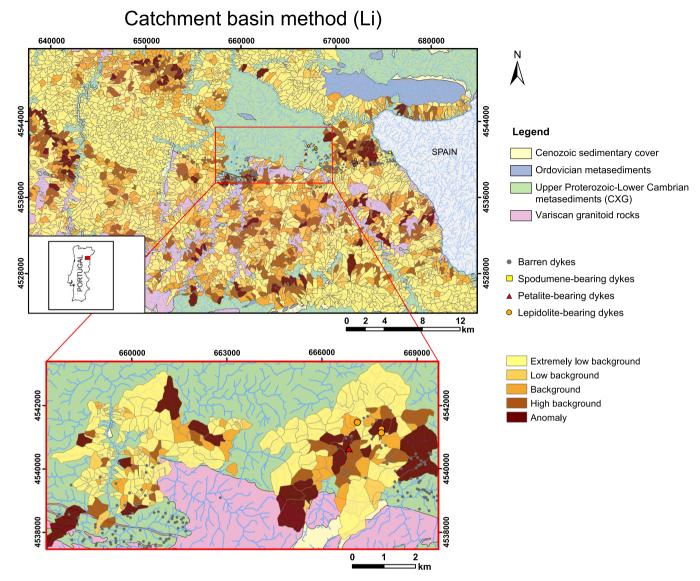
## Catchment basin method (Li)



**Fig. 6.** Spatial distribution of diluted-corrected Li residuals for the BRGM (top) and SFM (bottom) campaigns. The thresholds used to identify distinct populations and define the anomalies are based on the log-log plots of Fig. B1. A simplified geological map is presented for reference.

**Table 3**
Performance matrix for uni- and multi-elemental anomaly definition considering the mapped pegmatites.

| | | BRGM (catchment basins = 3362) | | SFM (catchment basins = 289) | |
|---|---|---|---|---|---|
| | | Intersecting known pegmatites | | Intersecting known pegmatites | |
| | | Li-rich | Barren | Li-rich | Barren |
| Uni-elemental | Anomalous | 4 | 5 | 5 | 6 |
| | Non-anomalous | 3 | 98 | 8 | 36 |
| | Overall accuracy (OA) | 93% | | 75% | |
| Multi-elemental | Highly Anomalous | 1 | 4 | 7 | 1 |
| | Other | 6 | 99 | 6 | 41 |
| | Overall accuracy (OA) | 91% | | 87% | |

representing a Sn—Li association, was 101 (around 3% of all catchment basins). The higher percentage of highlighted basins coupled with the lower OA of 91% indicates that the multi-elemental analysis did not produce the expected results, i.e., a decrease in the number of

anomalous basins and reduce granite influence. However, intersecting anomalous Sn—Li basins with the previously identified Li-anomalous areas, the total number of highlighted catchments drops to 39.

Oppositely, in the SFM campaign, the number of highly anomalous basins, representing a Sn-Li-B association, was only 13 (around 4.5% of all catchment basins). This multi-element strategy not only allowed to eliminate anomalous areas related to the granites but also to increase the number of anomalous basins intersecting known Li-pegmatites (Fig. 7). Consequently, the OA of the C-A fractal method employed to the PCA results of Li pathfinder elements increased to 87% comparing to 75% obtained in the uni-elemental anomaly definition. The importance of using multi-elemental strategies for Li-exploration had already been demonstrated in the works of Fyzollahhi et al. (2018), Saadati et al. (2020), where the association with elements such as Cs, Rb, F, Be, Sn, and Nb not only allowed to identify Li anomalous areas but also to discriminate two distinct Li-sources: (i) related to granites and pegmatites, and (ii) associated with Li-clays. The fact that the multi-elemental strategy was not equally successful in reducing the granites' influence in the BRGM campaign may indicate that in some cases the anomalous values are not just a consequence of the lithological background and that there can be anomalous areas inside the granites. This is out of the scope
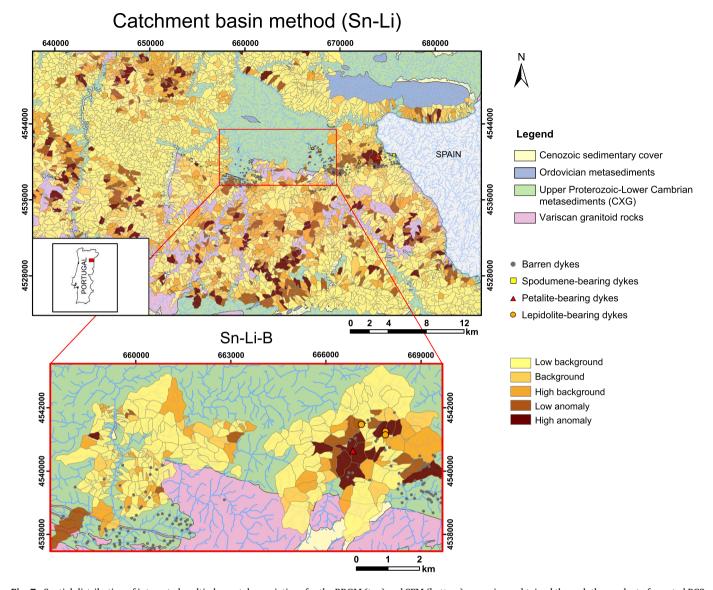
**Fig. 7.** Spatial distribution of integrated multi-elemental associations for the BRGM (top) and SFM (bottom) campaigns, obtained through the product of negated PC2 scores with PC4 scores, and the product of PC1 and PC2 scores, respectively (Tables B1 and B2). The thresholds used to identify distinct populations and define the anomalies are based on the log-log plots of Fig. B1. A simplified geological map is presented for reference.

of this work, but it is worth further investigation in future studies to try to evaluate if there is any economic interest within the granites.

The OA reflects the ability of the employed approach to highlight anomalous basins with known Li-pegmatites and disregard areas with barren dykes. However, the anomalous basins intersecting barren pegmatites are of interest and should be validated in the field in the case of hidden Li-mineralization, that is, in the case that Li-minerals are not observed in the pegmatite surface but occur at depth.

Comparing both approaches, it is evident that the catchment basin approach is more suitable for prospect scale exploration, since it allows to only target the areas covered by the catchment basins (lesser area than the clusters of Fig. 6). Nonetheless, this catchment method proved to be very time-consuming, dependent on distinct processing steps, and the anomaly definition through fractal analysis was not straightforward. Ideally, such an approach could only be employed in the target areas defined through the spatial interpolation method, thus optimizing the chain process along the different stages of exploration.

### 4.3. Field validation

Two field campaigns were conducted to validate the results of the spatial interpolation and catchment basin approaches. This validation was affected by three main constraints: (i) poor road accesses to the interest areas (that implied traveling great distances to visit nearby places); (ii) several interest areas were located inside fenced private propriety; and (iii) the rough terrain of the region that did not allow to check every pegmatite dyke within anomalous basins. Despite this, eleven basins were checked in the field. Due to the time limitation, preference was given to anomalous basins where the existence of pegmatite dykes is known. Consequently, 17 pegmatite dykes were inspected for possible Li-mineralization. Table 4 shows Rb and K/Rb values for measured K-feldspar crystal in the inspected pegmatite dykes, being high Rb contents and low K/Rb values indicative of higher fractionation degree of the pegmatite, and of high mineralization potential (Smeds, 1992).

In the region covered by the SFM campaign, it was possible to identify, in an anomalous area, one pegmatite dyke (previously mapped as barren) containing mineralization in Li and Sn (in the transition

**Table 4**

Comparison of the $K_2O$, Rb and K/Rb values obtained in K-feldspars of the analyzed aplite-pegmatite dykes with the measured and diluted-corrected residuals of Li in the respective catchment basin. For this purpose, only fresh K-feldspar crystals were considered ($K_2O > 8\%$). Rb contents above 2000 ppm are highlighted in bold indicating favorable evidence for Li-mineralization.

| Basin no. | Campaign | Measured Li (ppm) | Diluted-corrected residuals | $K_2O$ (%) | Rb (ppm) | K/Rb |
|---|---|---|---|---|---|---|
| 597 | BRGM | 177 | 59.78 | 12.06 | 1605 | 62.38 |
| | | | | 9.33 | 1111 | 69.74 |
| | | | | 8.99 | 1509 | 49.48 |
| | | | | 11.55 | 899 | 106.64 |
| | | | | 8.47 | 1751 | 40.13 |
| | | | | 9.93 | 1657 | 49.77 |
| 2277[a] | | 208 | 55.67 | 13.53 | **2798** | 40.14 |
| 4083 | | 135 | 4.07 | 10.21 | 1940 | 43.70 |
| 4102 | | 130 | 35.87 | 14.84 | 820 | 150.25 |
| | | | | 12.17 | 1099 | 91.94 |
| 4358 | SFM | 73 | 49.95 | 10.66 | 698 | 126.82 |
| | | | | 8.14 | **2934** | 23.03 |
| | | | | 8.53 | **2712** | 26.12 |
| 4361/4358 | | 95/73 | 28.43/49.95 | 10.47 | **3688** | 23.58 |
| 4361 | | 95 | 28.43 | 9.05 | **4376** | 17.16 |
| | | | | 8.29 | **2416** | 28.48 |
| | | | | 9.50 | **2575** | 30.63 |
| | | | | 14.74 | 1761 | 69.46 |
| | | | | 13.65 | **2737** | 44.00 |

[a] Classified as high background through the uni-elemental C-A fractal analysis.

between basins no. 4361 and 4358 of Table 4). The first occurs mainly in pink microcrystalline masses of Li-micas with occasional petalite skeletal relics (boxworks) visible in Fig. 8. The latter occurs in millimetric to centimetric cassiterite crystals containing small amounts of Nb and Ta. Iron and manganese phosphates were also found. Additionally, two other pegmatites in anomalous basins presented favorable evidence for Li-mineralization (Rb > 2000 ppm in K-feldspars), although no Li-mineralization was observed at the surface. Most pegmatite dykes were almost entirely covered by lichens which difficulted the recognition of possible Li-mineralization. It can also be the case that Li-minerals only occur at depth thus not allowing its recognition on outcrops even after using a hammer and sledgehammer to obtain vegetation-free samples. Moreover, the field campaigns allowed to identify a pegmatite dyke that was previously unknown (Fig. 8). These findings show the importance of stream sediment analysis and the use of portable tools in Li-pegmatite exploration.

For the BRGM campaign, less evidence of the source Li anomalies was found: all pegmatite dykes within anomalous basins visited in the field did not show favorable Rb and Li contents in K-feldspars (Table 4) and micas, respectively. Despite this, one pegmatite with the potential to be Li mineralized was identified within a catchment basin highlighted as high background through the uni-elemental C-A fractal analysis (basin no. 2277 of Table 4). To the south of the study area, the validated anomalous basins corresponded to: (i) urbanized areas, which may indicate human contamination, and (ii) granite-related areas. In the latter, intragranitic pegmatite dykes were observed, but presenting low Rb content in the K-feldspars and low Li content on the micas. Oppositely, the biotite in the granites showed higher relative Li contents than the ones observed in the pegmatites. Further studies may be employed in the future to assess the economic potential of Li within the granitoid
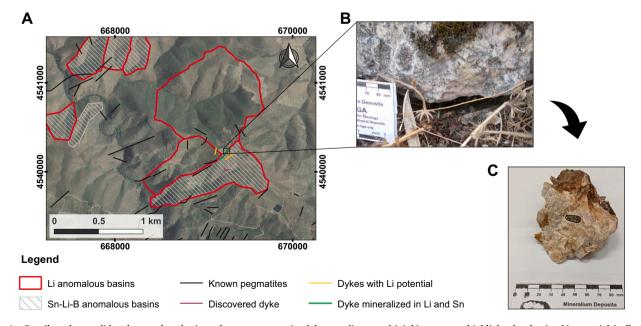


**Fig. 8.** A – Detail on three validated anomalous basins, where one pegmatite dyke was discovered (pink), two were highlighted as having Li potential (yellow), and where Li and Sn mineralization was found in a pegmatite previously considered as barren. B – Aspect of the Li mineralization in the outcrop (pink microcrystalline masses). C – Pink microcrystalline masses and boxworks of a previous petalite crystal in a hand sample. (For interpretation of the references to colour in this figure legend, the reader is referred to the web version of this article.)

rocks.

## 5. Conclusions

The performance of two distinct approaches to the geochemical exploration of Li-pegmatites was evaluated and the results have demonstrated their usefulness for this purpose:

1. The spatial interpolation method is a simple and expeditious approach for the early stages of mineral exploration (regional exploration). Despite the influence of granitoid rocks that can overshadow Li anomalous areas due to the occurrence of evolved pegmatites, it was possible to delineate smaller areas of interest for detailed studies. Future works should consider masking or other techniques to decrease the granites' influence.
2. Oppositely, the catchment basin approach proved to be an important tool for prospect scale exploration, allowing to mark smaller areas for field verification. Removing the influence of the geological background reduced the anomalous areas related to granites. To optimize the exploration campaigns, this approach could be employed in the areas previously defined through the spatial interpolation method, due to the great computational cost and complexity involved in this catchment area approach.
3. In both approaches, the use of key pathfinder elements was crucial to delineate target areas and discriminate granite-related from pegmatite-related Li anomalies. This was particularly true for the SFM campaign, where the elements selected showed correlations with Li in both CIZ's Li-rich bodies and the stream sediment samples, highlighting an important Sn-Li-B association. Other pathfinder elements could be used for Li exploration worldwide, namely Rb, Cs, and F.
4. Finally, the C-A fractal method was very effective in reducing the number of catchment basins to validate in the field which can be of great interest for exploration companies, allowing to reduce the costs and duration of field campaigns. The accuracy of this approach was high (>75%) when considering the previously mapped Li-pegmatites. The performance of the method was also confirmed through field validation. The fractal analysis allowed the identification of a pegmatite containing Li and Sn mineralization in one of the anomalous basins and highlights three other pegmatites with favorable evidence for possible hidden Li-mineralization.
5. Although multiple strategies were employed to reduce the granites' influence in the definition of anomalous basins, several areas persisted as anomalous. Therefore, further studies are needed to assess if there is any economic interest within the granites for Li.

## CRediT authorship contribution statement

**Joana Cardoso-Fernandes:** Conceptualization, Methodology, Software, Validation, Formal analysis, Investigation, Data curation, Writing – original draft, Visualization. **Jessica Lima:** Conceptualization, Methodology, Software, Validation, Formal analysis, Investigation, Data curation, Writing – review & editing. **Alexandre Lima:** Conceptualization, Methodology, Validation, Formal analysis, Resources, Writing – review & editing, Supervision, Project administration, Funding acquisition. **Encarnación Roda-Robles:** Conceptualization, Formal analysis, Resources, Writing – review & editing, Supervision, Funding acquisition. **Martin Köhler:** Methodology, Software, Formal analysis, Investigation, Data curation, Writing – review & editing. **Stefan Schaefer:** Methodology, Software, Formal analysis, Investigation, Data curation, Writing – review & editing. **Andreas Barth:** Methodology, Project administration. **Andreas Knobloch:** Methodology, Supervision, Project administration, Funding acquisition. **Mário A. Gonçalves:** Methodology, Software, Writing – review & editing. **Filipe Gonçalves:** Validation, Investigation, Writing – review & editing. **Ana Cláudia Teodoro:** Conceptualization, Resources, Writing – review & editing, Supervision, Funding acquisition.

## Declaration of competing interest

The authors declare that they have no known competing financial interests or personal relationships that could have appeared to influence the work reported in this paper.

## Supplementary data

Supplementary data to this article can be found online at https://doi.org/10.1016/j.gexplo.2022.106978.

## References

Almeida, C.M.P.d., 2003. In: Estudo do filão aplitopegmatítico da mina da Bajoca, Almendra: contribuição científico-tecnológica, XIV. Faculdade de Ciências da Universidade do Porto, Porto, p. 120.

Angel, J.M., Viallefond, L., 1981. In: Prospection géochimique Portugal. Résultats analytiques et interprétation de l'échantillonnage réalisé par le S.F.M. sur la feuille 15A, région de Almendra (NOTE/GMX-748), p. 6.

Antunes, I.M.H.R., Neiva, A.M.R., Ramos, J.M.F., Silva, P.B., Silva, M.M.V.G., Corfu, F., 2013. Petrogenetic links between lepidolite-subtype aplite-pegmatite, aplite veins and associated granites at Segura (central Portugal). Geochemistry 73, 323–341. https://doi.org/10.1016/j.chemer.2012.12.003.

Bonham-Carter, G.F., Rogers, P.J., Ellwood, D.J., 1987. Catchment basin analysis applied to surficial geochemical data, Cobequid Highlands, Nova Scotia. J. Geochem. Explor. 29, 259–278. https://doi.org/10.1016/0375-6742(87)90081-1.

Cardoso-Fernandes, J., Lima, A., Roda-Robles, E., Ribeiro, M.A., Teodoro, A., 2020a. Geochemical pathfinder analysis for lithium (Li) exploration in the Iberian Peninsula. In: Paper Presented at the X Congresso Jovens Investigadores em Geociências, LEG, Estremoz, pp. 12–15.

Cardoso-Fernandes, J., Teodoro, A.C., Lima, A., Mielke, C., Körting, F., Roda-Robles, E., Cauzid, J., 2020b. Multi-scale approach using remote sensing techniques for lithium pegmatite exploration: first results, 26 Sept.-2 Oct. 2020. In: Paper Presented at the IGARSS 2020 - 2020 IEEE International Geoscience and Remote Sensing Symposium, Waikoloa, HI, USA, pp. 5226–5229. https://doi.org/10.1109/IGARSS39084.2020.9323705.

Carranza, E.J.M., 2004. Usefulness of stream order to detect stream sediment geochemical anomalies, 4, 341–352. https://doi.org/10.1144/1467-7873/03-040.

Carranza, E.J.M., 2009a. Chapter 4: fractal analysis of geochemical anomalies. In: Carranza, E.J.M. (Ed.), Handbook of Exploration and Environmental Geochemistry. Elsevier Science B.V, pp. 85–114.

Carranza, E.J.M., 2009. Chapter 5: catchment basin analysis of stream sediment anomalies. In: Carranza, E.J.M. (Ed.), Handbook of Exploration and Environmental Geochemistry. Elsevier Science B.V., pp. 115–144

Carranza, E.J.M., Hale, M., 1997. A catchment basin approach to the analysis of reconnaissance geochemical - geological data from Albay province, Philippines. J. Geochem. Explor. 60, 151–171.

Carvalhosa, A., 1960. Carta Geológica de Portugal na escala 1/50.000 – folha 15-D – Figueira de Castelo Rodrigo. Serviços Geológicos de Portugal, Lisboa, Portugal.

Černý, P., Ercit, T.S., 2005. Classification of granitic pegmatites revisited. Can. Mineral. 43, 2005–2026.

Cerny, P., Meintzer, R.E., Anderson, A.J., 1985. Extreme fractionation in rare-element granitic pegmatites; selected examples of data and mechanisms. Can. Mineral. 23, 381–421.

Charoy, B., Noronha, F., 1996. Multistage growth of a rare-element, volatile-rich microgranite at Argemela (Portugal). J. Petrol. 37, 73–94. https://doi.org/10.1093/petrology/37.1.73.

Cheng, Q., Agterberg, F.P., Ballantyne, S.B., 1994. The separation of geochemical anomalies from background by fractal methods. J. Geochem. Explor. 51, 109–130. https://doi.org/10.1016/0375-6742(94)90013-2.

<collab>Environmental Systems Research Institute, I.</collab>, 2020. ArcMap Software.

Costa, J.C.S.d., 1950. Notícia sobre uma carta geológica do Buçaco, de Nery Delgado, 26 Sept.-2 Oct. 2020. Serviços Geológicos de Portugal, Lisboa, Portugal.

Díez Balda, M.A., Vegas, R., Lodeiro, G., 1990. Central Iberian Zone: structure. In: Dallmeyer, R.D., Martinez Garcia, E. (Eds.), Pre-Mesozoic Geology of the Iberian Peninsula. Springer Verlag, Berlim, pp. 172–188.

Dill, H.G., Weber, B., Melcher, F., Wiesner, W., Müller, A., 2014. Titaniferous heavy mineral aggregates as a tool in exploration for pegmatitic and aplitic rare-metal deposits (SE Germany). Ore Geol. Rev. 57, 29–52. https://doi.org/10.1016/j.oregeorev.2013.08.023.

European Commission: DG Internal Market Industry Entrepreneurship and SMEs, 2020. In: Critical Raw Materials Resilience: Charting a Path towards greater Security and Sustainability (COM(2020) 474 Final). Brussels, p. 23.

Fabre, C., Ourti, N.E., Mercadier, J., Cardoso-Fernandes, J., Dias, F., Perrotta, M., Koerting, F., Lima, A., Kaestner, F., Koellner, N., Linnen, R., Benn, D., Martins, T., Cauzid, J., 2021. Analyses of Li-rich minerals using handheld LIBS tool. Data 6, 68. https://doi.org/10.3390/data6060068.

Ferreira, J.A., Bento dos Santos, T., Pereira, I., Mata, J., 2019. Tectonically assisted exhumation and cooling of Variscan granites in an anatectic complex of the Central Iberian Zone, Portugal: constraints from LA-ICP-MS zircon and apatite U-Pb ages. Int. J. Earth Sci. 108, 2153–2175. https://doi.org/10.1007/s00531-019-01755-1.

Ferreira, J.A., Mata, J., Bento dos Santos, T., Pereira, I., 2020. The role of melting on the geochemical evolution and isotopic variability of an anatectic complex in the Iberian Variscides. Lithos 378–379, 105769. https://doi.org/10.1016/j.lithos.2020.105769.

Frick, C., Strauss, S.W., 1987. Geochemical evolution of the Richtersveld area, South Africa, as deduced from regional geochemical maps of stream sediments. J. Geochem. Explor. 28, 431–449. https://doi.org/10.1016/0375-6742(87)90061-6.

Fuertes Fuente, M., Martin Izard, A., 1998. The Forcarei Sur rare-element granitic pegmatite field and associated mineralization, Galicia, Spain. Can. Mineral. 36, 303–325.

Fyzollahhi, N., Torshizian, H., Afzal, P., Jafari, M.R., 2018. Determination of lithium prospects using fractal modeling and staged factor analysis in Torud region, NE Iran. J. Geochem. Explor. 189, 2–10. https://doi.org/10.1016/j.gexplo.2017.09.017.

Gallego Garrido, M., 1992. In: Las mineralizaciones de Li asociadas a magmatismo ácido en Extremadura y su encuadre en la Zona Centro-Ibérica. Universidad Complutense de Madrid, Madrid, Spain, p. 323.

George, H., Bonham-Carter, G.F., 1989. Spatial modeling of geological data for gold exploration, Star Lake area, Saskatchewan. In: Agterberg, F.P., Bonham-Carter, G.F. (Eds.), Statistical Application in the Earth Sciences. Geological Survey of Canada Paper 89-9, pp. 157–169.

Ghezelbash, R., Maghsoudi, A., 2018. Comparison of U-spatial statistics and C-A fractal models for delineating anomaly patterns of porphyry-type Cu geochemical signatures in the Varzaghan district, NW Iran. Compt. Rendus Geosci. 350, 180–191. https://doi.org/10.1016/j.crte.2018.02.003.

Ghezelbash, R., Maghsoudi, A., Carranza, E.J.M., 2019. An improved data-driven multiple criteria decision-making procedure for spatial modeling of mineral prospectivity: adaption of prediction-area plot and logistic functions. Nat. Resour. Res. 28, 1299–1316. https://doi.org/10.1007/s11053-018-9448-6.

Gonçalves, M.A., Mateus, A., Oliveira, V., 2001. Geochemical anomaly separation by multifractal modelling. J. Geochem. Explor. 72, 91–114. https://doi.org/10.1016/S0375-6742(01)00156-X.

Hawkes, H.E., 1976. The downstream dilution of stream sediment anomalies. J. Geochem. Explor. 6, 345–358. https://doi.org/10.1016/0375-6742(76)90023-6.

Helal, B., 1992. In: Granitoïdes, granites à métaux rares et hydrothermalisme associé. Géologie, minéralogie et géochimie de plusieurs suites tardi-hercyniennes (Nord du Portugal). Ecole Nationale Supérieure des Mines de Paris, p. 507.

Johnston, K., Ver Hoef, J., Krivoruchko, K., Lucas, N., 2004. Using ArcGIS Geostatistical Analyst. ESRI Press.

Kaeter, D., Menuge, J.F., Harrop, J., 2019. Stream sediment geochemistry for regional prospectivity analysis: Tin, cesium, tantalum and tungsten anomalies in Leinster, southeast Ireland, 27-30 August 2019. In: Paper Presented at the Proceedings of the 15th SGA Biennial Meeting, Glasgow, Scotland, pp. 1228–1231.

Kesler, S.E., Gruber, P.W., Medina, P.A., Keoleian, G.A., Everson, M.P., Wallington, T.J., 2012. Global lithium resources: Relative importance of pegmatite, brine and other deposits. Ore Geol. Rev. 48, 55–69. https://doi.org/10.1016/j.oregeorev.2012.05.006.

Köhler, M., Hanelli, D., Schaefer, S., Barth, A., Knobloch, A., Hielscher, P., Cardoso-Fernandes, J., Lima, A., Teodoro, A.C., 2021. Lithium potential Mapping using Artificial Neural Networks: a Case Study from Central Portugal. Minerals 11, 1046. https://doi.org/10.3390/min11101046.

Leal Gomes, C., 1994. In: Estudo estructural e paragenético de um sistema pegmatóide granítico. O campo aplito-pegmatítico de Arga Minho, Portugal. Universidade do Minho, p. 695.

Marroncle, J.L., 1980. In: Consórcio SPE/SEREM: Relatório semestral (Abril 1980-Novembro 1980), p. 44. Unpublished.

Marroncle, J.L., 1980. In: Consórcio SPE/SEREM: Relatório semestral (Novembro 1979 - Abril 1980), p. 44. Unpublished.

Martínez Catalán, J.R., Martínez Poyatos, D., Bea, F., 2004. Zona Centroibérica: Introducción. In: Vera, J.A. (Ed.), Geología de España. Sociedad Geológica de España/Instituto Geológico y Minero de España (SGE-IGME), Madrid, pp. 68–69.

Martín-Izard, A., Reguilón, R., Palero, F., 1992. Las mineralizaciones litiníferas del oeste de Salamanca y Zamora. Estud. Geol. 48, 19–30.

Melleton, J., Gloaguen, E., Frei, D., Lima, A., 2011. U-Pb dating of columbite-tantalite from Variscan rare-elements granites and pegmatites, 2011-08-14. In: Paper Presented at the Goldschmidt 2011, Prague, Czech Republic, p. 1452.

Mokhtari, A.R., Garousi Nezhad, S., 2015. A modified equation for the downstream dilution of stream sediment anomalies. J. Geochem. Explor. 159, 185–193. https://doi.org/10.1016/j.gexplo.2015.09.007.

Mukaka, M.M., 2012. Statistics corner: a guide to appropriate use of correlation coefficient in medical research. Malawi Med. J. 24, 69–71.

Négrel, P., Ladenberger, A., Reimann, C., Birke, M., Demetriades, A., Sadeghi, M., 2019. GEMAS: Geochemical background and mineral potential of emerging tech-critical elements in Europe revealed from low-sampling density geochemical mapping. Appl. Geochem. 111, 104425 https://doi.org/10.1016/j.apgeochem.2019.104425.

Neiva, A.M.R., Ramos, J.M.F., 2010. Geochemistry of granitic aplite-pegmatite sills and petrogenetic links with granites, Guarda-Belmonte area, Central Portugal. Eur. J. Mineral. 22, 837–854. https://doi.org/10.1127/0935-1221/2010/0022-2072.

Pereira, I., Dias, R., Bento dos Santos, T., Mata, J., 2017. Exhumation of a migmatite complex along a transpressive shear zone: inferences from the Variscan Juzbado-Penalva do Castelo Shear Zone (Central Iberian Zone). J. Geol. Soc. 174, 1004. https://doi.org/10.1144/jgs2016-159.

Pérez-Estaún, A., Bea, F., Bastida, F., Marcos, A., Martínez Catalán, J.R., Martínez Poyatos, D., Arenas, R., Díaz García, F., Azor, A., Simancas, J.F., González Lodeiro, F., 2004. La cordillera varisca europea: el Macizo Ibérico. In: Vera, J.A. (Ed.), Geología de España. Sociedad Geológica de España/Instituto Geológico y Minero de España (SGE-IGME), Madrid, pp. 21–25.

Ribeiro, M.L., 2001. Notícia explicativa da carta geológica simplificada do Parque Arqueológico do Vale do Côa. Parque Arqueológico do Vale do Côa, Vila Nova de Foz Côa, Portugal.

Ribeiro, M.L., Silva, A.F., 2000. Carta Geológica Simplificada do Parque Arqueológico do Vale do Côa. Instituto Geológico e Mineiro and Parque Arqueológico do Vale do Côa, Vila Nova de Foz Côa, Portugal.

Ribeiro, R., Lima, A., Guimarães, D., 2018. Concentrations of Rb in K-feldspar from the pegmatite-aplite Barroso-Alvão Field. In: Paper Presented at the VIII Congresso Jovens Investigadores em Geociências, LEG, Livro de Actas Estremoz, pp. 50–53.

Roda, E., 1993. In: Distribución, Caracteristicas y Petrogenesis de las Pegmatitas de La Fregeneda (Salamanca). Dep. Min. y Petrol. Facultad de Ciencia y Tecnología de la Universidad del País Vasco (UPV/EHU), Bilbao, Spain, p. 199.

Roda-Robles, E., Pesquera, A., Velasco, F., Fontan, F., 1999. The granitic pegmatites of the Fregeneda area (Salamanca, Spain): characteristics and petrogenesis. Mineral. Mag. 63, 535–558.

Roda-Robles, E., Vieira, R., Pesquera, A., Lima, A., 2010. Chemical variations and significance of phosphates from the Fregeneda-Almendra pegmatite field, Central Iberian Zone (Spain and Portugal). Mineral. Petrol. 100, 23–34. https://doi.org/10.1007/s00710-010-0117-7.

Roda-Robles, E., Pesquera, A., Gil-Crespo, P., Torres-Ruiz, J., 2012. From granite to highly evolved pegmatite: a case study of the Pinilla de Fermoselle granite–pegmatite system (Zamora, Spain). Lithos 153, 192–207. https://doi.org/10.1016/j.lithos.2012.04.027.

Roda-Robles, E., Pesquera, A., Gil-Crespo, P.P., Vieira, R., Lima, A., Garate-Olave, I., Martins, T., Torres-Ruiz, J., 2016. Geology and mineralogy of Li mineralization in the Central Iberian Zone (Spain and Portugal). Mineral. Mag. 80, 103–126. https://doi.org/10.1180/minmag.2016.080.049.

Roda-Robles, E., Villaseca, C., Pesquera, A., Gil-Crespo, P.P., Vieira, R., Lima, A., Garate-Olave, I., 2018. Petrogenetic relationships between Variscan granitoids and Li-(F-P)-rich aplite-pegmatites in the Central Iberian Zone: Geological and geochemical constraints and implications for other regions from the European Variscides. Ore Geol. Rev. 95, 408–430. https://doi.org/10.1016/j.oregeorev.2018.02.027.

Rodríguez Alonso, M.D., Díez Balda, M.A., Perejón, A., Pieren, A., Liñán, E., López Díaz, F., Moreno, F., Gámez Vintaned, J.A., Gónzalez Lodeiro, F., Martínez Poyatos, D., Vegas, R., 2004. Domínio del Complejo Esquisto-Grauváquico: Estratigrafía. La secuencia litoestratigráfica del Neoproterozóico-Câmbrico Inferior. In: Vera, J.A. (Ed.), Geología de España. Geol. España/Inst. Geol. Min. España (SGE-IGME), Madrid, pp. 78–81.

Rose, A.W., Hawkes, H.E., Webb, J.S., 1979. Geochemistry in Mineral Exploration. Academic Press, London.

Saadati, H., Afzal, P., Torshizian, H., Solgi, A., 2020. Geochemical exploration for lithium in NE Iran using the geochemical mapping prospectivity index, staged factor analysis, and a fractal model. Geochem. Explor. Environ. Anal. 20, 461–472. https://doi.org/10.1144/geochem2020-020.

San José, M.A., Pieren, A.P., Garcia-Hidalgo, J.F., Vilas, L., Herranz, P., Pelaez, J.R., Perejon, A., 1990. Central Iberian Zone. Autochthonous sequences: Ante-Ordovician stratigraphy. In: Dallmeyer, R.D., Martinez Garcia, E. (Eds.), Pre-Mesozoic Geology of Iberia. Springer-Verlag, Berlin, Heidelberg, pp. 147–159.

Shahrestani, S., Mokhtari, A.R., 2017. Improved detection of anomalous catchment basins by incorporating drainage density in dilution correction of geochemical residuals. Geochem. Explor. Environ. Anal. 17, 194–203. https://doi.org/10.1144/geochem2016-015.

Shepard, D., 1968. A two-dimensional interpolation function for irregularly-spaced data. In: Proceedings of the 1968 23rd ACM National Conference. Association for Computing Machinery, pp. 517–524.

Silva, A.F., 2005. A Litostratigrafia e Estrutura do Supergrupo Dúrico-Beirão (Complexo Xisto-Grauváquico), em Portugal, e sua Correlação com as Correspondentes

Sucessões em Espanha. Instituto Nacional de Engenharia, Tecnologia e Inovação, IP, Alfragide, Portugal.

Silva, A.F.d., Ribeiro, M.L., 1991. Notícia Explicativa da folha 15-A Vila Nova de Foz Côa. Serviços Geológicos de Portugal, Lisboa, Portugal.

Silva, A.F.d., Ribeiro, M.L., 1994. Notícia Explicativa da folha 15-B Freixo de Espada à Cinta. Instituto Geológico e Mineiro, Lisboa, Portugal.

Silva, A.F.d., Rebelo, J.A., Ribeiro, M.L., 1989. Notícia Explicativa da folha 11-C Torre de Moncorvo. Serviços Geológicos de Portugal, Lisboa, Portugal.

Silva, A.F., Santos, A.J., Ribeiro, A., Cabral, J., Ribeiro, M.L., 1990. Carta Geológica de Portugal na escala 1/50.000 – folha 15-B – Freixo de Espada à Cinta. Serviços Geológicos de Portugal, Lisboa, Portugal.

Silva, A.F., Santos, A.J., Ribeiro, A., Ribeiro, M.L., 1990. Carta Geológica de Portugal na escala 1/50.000 – folha 15-A – Vila Nova de Foz Côa. Serviços Geológicos de Portugal, Lisboa, Portugal.

Silva, A.F., Romão, J.M.C., Sequeira, A.J.D., Oliveira, J.T., 1995. A sucessão litostratigráfica anté-ordovícica na Zona Centro-Ibérica (ZCI), em Portugal: Ensaio de interpretação com base nos dados actuais. In: Paper Presented at the XIII Reunión de Geología del Oeste Peninsular, RGOP/PICG, 319-320, Univ. Salamanca, Salamanca, pp. 71–72.

Simmons, W.B.S., Webber, K.L., 2008. Pegmatite genesis: state of the art. Eur. J. Mineral. 20, 421–438. https://doi.org/10.1127/0935-1221/2008/0020-1833.

Smeds, S.A., 1992. Trace elements in potassium-feldspar and muscovite as a guide in the prospecting for lithium- and tin-bearing pegmatites in Sweden. J. Geochem. Explor. 42, 351–369. https://doi.org/10.1016/0375-6742(92)90032-4.

Sousa, M.B., 1982. In: Litostratigrafia e estrutura do "Complexo Xisto-Grauváquico Ante-Ordovícico" – Grupo do Douro (Nordeste de Portugal). Centro de Geociências da Universidade de Coimbra, Coimbra, Portugal, p. 222.

Sousa, M.B., 1983. In: Considerações paleogeográficas e ensaio de correlação das formações do Grupo do Douro (CXG) com as formações ante-Ordovícicas da Zona Centro-Ibérica, 65. Memórias e Notícias, Publicações do Museu e Laboratório Mineralógico e Geológico da Universidade de Coimbra, pp. 65–98.

Sousa, M.B., 1984. Considerações sobre a estratigrafia do Complexo Xisto-Grauváquico (CXG) e sua relação com o Paleozóico Inferior. Cuad. Geol. Iber. 9, 9–36.

Spadoni, M., 2006. Geochemical mapping using a geomorphologic approach based on catchments. J. Geochem. Explor. 90, 183–196. https://doi.org/10.1016/j.gexplo.2005.12.001.

Steiner, B., 2018. Using Tellus stream sediment geochemistry to fingerprint regional geology and mineralisation systems in Southeast Ireland. Irish J. Earth Sci. 36, 45–61. https://doi.org/10.3318/ijes.2018.36.45.

Steiner, B.M., 2019. W and Li-Cs-Ta geochemical signatures in I-type granites – a case study from the Vosges Mountains, NE France. J. Geochem. Explor. 197, 238–250. https://doi.org/10.1016/j.gexplo.2018.12.009.

Steiner, B.M., Rollinson, G.K., Condron, J.M., 2019. An Exploration Study of the Kagenfels and Natzwiller Granites, Northern Vosges Mountains, France: a combined Approach of Stream Sediment Geochemistry and Automated Mineralogy. Minerals 9, 750. https://doi.org/10.3390/min9120750.

Strahler, A.N., 1952. Hypsometric (Area-Altitude) analysis of erosional topography. GSA Bull. 63, 1117–1142. https://doi.org/10.1130/0016-7606(1952)63[1117:Haaoet]2.0.Co;2.

Teixeira, C., 1955. Notas sobre geologia de Portugal o complexo xisto-grauváquico ante-ordoviciano. Empresa Literaria Fluminense Lda, Lisboa, Portugal.

Viallefond, L., 1981. In: Prospection géochimique Portugal: Résultats analytiques et interprétation de l'échantillonnage réalisé par le S.F.M. sur la feuille 15B (NOTE/GMX-732), p. 27.

Viallefond, L., Angel, J.M., 1981. In: Portugal Nord - Feuille 15A-15C - Interprétation des données analytiques (NOTE/GMX-738), p. 17.

Viegas, L., Lima, L.P., Soares, J., Fonseca, E.C., 1983–85. Aplicação da análise estatística multi-variada ao estudo de amostras de sedimentos na região de Escalhão- Barca D'Alva (NE de Portugal). In: Boletim da Sociedade Geológica de Portugal XXIV, pp. 161–169.

Vieira, R., 2010. Aplitopegmatitos com elementos raros da região entre Almendra (V.N. de Foz Côa) e Barca d'Alva (Figueira de Castelo Rodrigo). In: Campo aplitopegmatítico da Fregeneda- Almendra. Faculdade de Ciências da Universidade do Porto, Porto, Portugal, XXVI, p. 273.

Vieira, R., Roda-Robles, E.n., Pesquera, A., Lima, A., 2011. Chemical variation and significance of micas from the Fregeneda-Almendra pegmatitic field (Central-Iberian Zone, Spain and Portugal). American Mineralogist 96, 637–645. https://doi.org/10.2138/am.2011.3584.

Von Knorring, O., Vidal Romani, J.R., 1981. In: On the mineralogy of the O Casteliño spodumene pegmatite near Lalín, Galicia Spain. Cadernos do Laboratorio Xeolóxico de Laxe, 2, pp. 259–262.

Zuo, R., 2011. Identifying geochemical anomalies associated with Cu and Pb–Zn skarn mineralization using principal component analysis and spectrum–area fractal modeling in the Gangdese Belt, Tibet (China). J. Geochem. Explor. 111, 13–22. https://doi.org/10.1016/j.gexplo.2011.06.012.